Electro-thermally induced structural failure actuator (ETISFA) for implantable controlled drug delivery devices based on Micro-Electro-Mechanical-Systems†

N. M. Elman,*[acd] B. C. Masi,[bd] M. J. Cima[acd] and R. Langer[bd]

Received 16th April 2010, Accepted 19th July 2010
DOI: 10.1039/c005135g

A new electro-thermally induced structural failure actuator (ETISFA) is introduced as an activation mechanism for on demand controlled drug delivery from a Micro-Electro-Mechanical-System (MEMS). The device architecture is based on a reservoir that is sealed by a silicon nitride membrane. The release mechanism consists of an electrical fuse constructed on the membrane. Activation causes thermal shock of the suspended membrane allowing the drugs inside of the reservoir to diffuse out into the region of interest. The effects of fuse width and thickness were explored by observing the extent to which the membrane was ruptured and the required energy input. Device design and optimization simulations of the opening mechanism are presented, as well as experimental data showing optimal energy consumption per fuse geometry. *In vitro* release experiments demonstrated repeatable release curves of mannitol-C^{14} that precisely follow ideal first order release kinetics. Thermally induced structural failure was demonstrated as a feasible activation mechanism that holds great promise for controlled release in biomedical microdevices.

Introduction

Implantable drug delivery devices based on MEMS (Micro-Electro-Mechanical-Systems) represent the next generation of smart micro delivery systems. A number of MEMS drug delivery devices have recently been described for treatment of both chronic and acute conditions.[1] The ability to selectively release drugs from implantable drug delivery devices on demand provides a means for complex and sustained release. Unique pharmacokinetic profiles can be designed and customized according to specific drugs and individual patient needs and can potentially overcome pharmacokinetic limitations of certain drugs. These MEMS drug delivery devices have been investigated as long term solutions for treatment of chronic illnesses, such as cancer, diabetes, as well as pain management.[2–4] Preventive medical care could be accomplished with this technology by creating autonomous device activation logic that is triggered by physiological signals.

A broad range of drug delivery rates can be accomplished by MEMS based micro delivery systems depending on what mechanism is utilized for mass efflux. Slow and intermediate rates can be accomplished by mechanisms such as diffusion or osmotic effects. Rapid rates have been accomplished by utilizing bubble nucleation to eject liquid from the device reservoir.[5] Other reports of MEMS drug delivery systems include subcutaneous implants for vasopressin delivery, multi-peptide delivery, as well as current investigation of delivery of chemotherapeutics for treatment of solid tumors, *i.e.* brain cancer.[6–10]

A major hurdle to the successful implementation of long term drug delivery devices that provide critical doses at the specific site of interest is, however, the overall miniaturization of the device. The common denominator for all MEMS drug delivery devices is their dependence on selective activation of opening mechanisms to release the drugs from isolated reservoirs. Several opening mechanisms have been investigated and reduced to practice, such as the use of electro-chemical degradation,[11] as well as electrical activation.[12,13] Electrical activation has proven to be the most effective, reliable mechanism, and therefore the most logical choice for integration with VLSI (very large scale integration) circuits, albeit the one choice that consumes the most energy.

One of the most critical parameters associated with the overall successful biomedical device implementation is the power consumption. Current battery technologies aim to optimize the energy–volume efficiency[14–16] to reduce the overall form factor, with capabilities of energy volume densities in range of 90–120 W h kg^{-1}, whereas state-of-art technologies aim for a 200–400 W h kg^{-1} range. The energy consumption of the device, therefore, defines a major portion of device volume as it is limited by the maximum energy density of the power source.

Reducing the overall energy consumption and size of the MEMS drug delivery device is the main motivation of this work. Previous generations of the MEMS drug delivery device that consisted of a full metallic membrane required 1 J for activation. The devices presented in this work require between 14 μJ and 1400 μJ for activation, a significant improvement. Existing battery technologies meet the requirements for powering these devices. Hence, reducing the overall device energy requirements linearly reduces the required battery mass and thus overall device

[a]*Department of Materials Science and Engineering, Massachusetts Institute of Technology, Cambridge, MA, USA. E-mail: nelman@mit.edu*
[b]*Department of Chemical Engineering, Massachusetts Institute of Technology, Cambridge, MA, USA*
[c]*Institute for Soldier Nanotechnologies, Massachusetts Institute of Technology, Cambridge, MA, USA*
[d]*Koch Institute for Integrative Cancer Research, Massachusetts Institute of Technology, 77 Massachusetts Ave., Room 12-002A, Cambridge, MA, USA*

† Electronic supplementary information (ESI) available: Diffusion profile derivation. See DOI: 10.1039/c005135g.

volume. Analogous fuse mechanisms for microfluidics were recently utilized for one-time use valves for controlling flow.[17,18] That work demonstrated that metallic fuses can effectively induce structural failure of membranes, but was limited to the millimetre scale and did not characterize the effects of the fuse cross-sectional geometry on activation.

The premise of this work is therefore the design of an opening mechanism for miniaturized implantable drug delivery devices capable of on demand activation for controlled release at low energy consumption. This electro-thermal induced failure actuator has been denominated ETISFA. The opening mechanism is a thin metallic fuse that spans a suspended membrane structure that isolates the contents of the device reservoir from the environment. The fuse is geometrically laid out on the structurally weakest point of the membrane. Activation causes rapid resistive heating of the fuse material, creating large stresses on the suspended structure leading to membrane rupture and reservoir exposure. The energy consumption for the ETISFA used for the *in vitro* release is approximately 134 μJ. This is an improvement of approximately 4 orders of magnitude over the previous device generation, which consisted of a full gold membrane of equivalent dimensions. The role of fuse width and thickness was closely studied in this work. The primary metrics for activation were the extent to which the membrane was ruptured and energy requirements for achieving rupture. The device design, model, and fabrication are presented here, followed by an experimental optimization to explore the role of fuse geometry. *In vitro* experiments showing the tightly controlled release are presented and discussed in detail.

Design of drug delivery device

The drug delivery device architecture consists of a modular design with three components: a reservoir, a sealing layer, and base port layer, as shown in Fig. 1. The reservoir provides the constrained space where the drugs are stored in either liquid or solid form, generally in the 20–100 μL range depending on the application and the potency of the required drug. The base layer provides an orifice that can be used to fill the device during fabrication. This orifice is later irreversibly sealed. The sealing layer insulates the drugs from the exterior, and contains the active portions of the device. The opening mechanism is defined as a metallic fuse deposited on a suspended silicon nitride membrane. Silicon nitride (Si_3N_4) was chosen as an insulating layer as it provides an excellent diffusion barrier, is biocompatible, and has robust mechanical properties to withstand manipulation and eventual implantation.[19–22] The activation mechanism is based on Joule heating. Electric power dissipated in the fuse is converted to heat, which increases the temperature of the fuse and membrane materials. The short electric pulse provides enough energy to melt the fuse and abruptly expand the membrane. The melting energy of the fuse material is defined by the following equation:

$$E_{\text{melt}} = c_{\text{p}}\rho lwh(T_{\text{f}} - T_{\text{o}}) + l_{\text{f}}\rho lwh \quad (1)$$

where c_{p} is the specific heat capacity, ρ is the material density, l is the length, w is the width, h is the thickness, T_{f} is the melting temperature, T_{o} is room temperature, and l_{f} is the latent heat of fusion.

The short energy pulse dramatically induces high strain levels on the suspended membrane due to the heat expansion of the silicon nitride. The resulting stress levels exceed the ultimate stress of the membrane, leading the silicon nitride to strain to the breaking point, shattering into small submicron fragments, which do not cause any apparent harm to the body.[23] Several fuse mechanism models have already been comprehensively formulated both analytically and numerically.[24,25] Our design goal is to first obtain a qualitative model for which it is possible to understand how the fuse dimensions affect the structure of the silicon nitride membrane, providing a general guidance for subsequent experiments. The total energy supplied by an electric pulse can be approximated by the following equation:

$$E_{\text{total}} = \frac{V^2 wh}{rl\alpha\left((T_{\text{m}} - T_{\text{o}}) + 1\right)}t \quad (2)$$

where V is the applied voltage, r is the resistivity, l is the length, w is the width, and h is the thickness, α is the thermal coefficient of expansion, T_{o} is the room temperature, T_{m} is the melting temperature of the fuse material, and t is the time of the applied pulse. The time can be defined by the Fourier number, a dimensionless parameter that is a measure of heat conducted through a body relative to the heat stored, given by the following equation:[26,27]

$$F_{\text{o}} = \frac{k_{\text{t}}t}{c_{\text{p}}\rho l_{\text{c}}^2} \quad (3)$$

where k_{t} is the heat conductance of the material, ρ is the material density, l_{c} is the critical dimension of interest, which in this case is the length of the gold fuse, and t is the time. A Fourier number of 0.1 was selected for the case where the energy dissipated is maximized.[26,27] The design trade-off is based on the optimization of structure dimensions as a decrease in the fuse cross-sectional area allows for an increase in the heat dissipation at the expense of a higher current density. The optimization, therefore, relies on

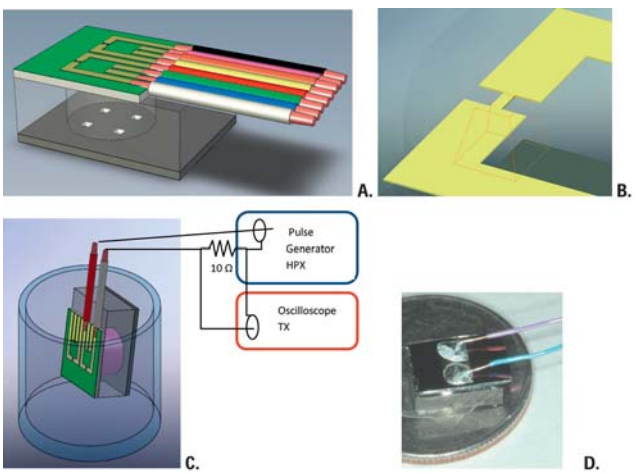

Fig. 1 (A) Render of the low power drug delivery device showing the three components: reservoir (translucent), sealing layer (green), and input port (gray). (B) Close-up of the fuse device. The fuse is the thin gold strip that bridges the larger gold strips over the membrane (not shown). (C) Experimental set-up for activation and controlled release. (D) Photograph of the device.

finding the right fuse dimensions that would provide enough Joule heating to reliably break the silicon nitride membrane.

A finite element analysis (FEA) based on CosmosWorks (SolidWorks, USA) was implemented to model the membrane structure for 3 different fuse types. The FEA provides stress and deformation maps in a static model for simplified analyses. A solid mesh was defined as approximately 10^5 elements for the each structure. Von Mises stresses were simulated as the structure was subjected to the melting temperature of Au uniformly along the metallic strip. The heat transfer to the bulk silicon and surrounding water and tissue was not simulated in this simplified simulation approach.

We first define the structural dimensions for the suspended low stress silicon nitride square membranes as 80 μm wide and 200 nm thick. The fuse is laid out across the center of the membrane, providing a symmetrical geometry for actuation. The fuse is defined as a bilayer strip conductor of titanium and gold. A 30 nm thick titanium layer is required to provide an adhesion layer for the gold. Two large electric pads on either side of the fuse allow energy to be delivered to the fuse from an external signal generator with very low parasitic losses. The dimensions of the strip are varied in the analysis in order to obtain a qualitative understanding of the effect on the membrane. The width of the gold is simulated as 20 μm, 40 μm, and 60 μm. A 3D render of fuse device is shown in Fig. 1B. Table 1 provides a summary of the material properties for energy calculation. Table 2 provides the pulse width and energy values as a function of fuse type, combining eqn (1)–(3). The factor of safety defined as the ratio of the Von Misses stress to the yield strength of the Si_3N_4 was monitored for the three cases. The thickness of the conductor is not relevant in this static simulation scenario as the temperature is statically defined on the fuse surface area, and this dimension does not play a role in the heat transfer process to the membrane. Von Mises stress maps and displacement views for each simulated structure are shown in Fig. 2.

The high stress levels are depicted in red. The simulations and calculations predict that as the fuse width is reduced, less energy is required to burst the membrane and as the fuse thickness is reduced, the current density is increased. The calculations and simulations demonstrate that the energy requirement will decrease with decreasing thickness and width. The optimal fuse dimensions, however, would allow both reaching the melting point of the gold structure and creating a mechanical failure mode sufficient to burst the entire membrane at the minimum energy. FEA results combined with the simple analytical model provide a preliminary baseline for the experimental assessment. The extent of the membrane rupture will be determined experimentally.

Table 1 Parameters and corresponding values used for analytical and numerical simulations. Values obtained from ref. 18, 20, 21, 30, 32, 33 and 35–40

#	Parameter	Description	Values	Units
1	l_m	Membrane length	80	μm
2	h_m	Membrane thickness	200	Nm
3	L	Fuse length	80	μm
4	W	Fuse width	20, 40, 60	μm
5	H	Fuse thickness	100, 250, 500	Nm
6	E_{sin}	Si_3N_4Young's modulus	310	GPa
7	S_{sin}	Shear modulus	260	GPa
8	ρ_{sin}	Si_3N_4 material density	3310	kg m^{-3}
9	T_{sin}	Si_3N_4 tensile stress	400	MPa
10	Y_{sin}	Si_3N_4 yield strength	4	GPa
11	k_{sin}	Si_3N_4 thermal conductivity	27	W m^{-1} K^{-1}
12	c_{p_sin}	Si_3N_4 heat capacity	710.6	J kg^{-1} K^{-1}
13	υ_{sin}	Si_3N_4 Poisson's ratio	0.23	—
14	α_{sin}	Si_3N_4—coeff. thermal expan.	3.3×10^{-6}	1 K^{-1}
15	r_{au}	Au electrical resistivity	2.24×10^{-8}	Ω m
16	α_{au}	Au—coeff. thermal expan.	1.4×10^{-5}	1 K^{-1}
17	E_{au}	Au Young's modulus	78	GPa
18	υ_{au}	Au Poisson's ratio	0.44	—
19	S_{au}	Au shear modulus	26	GPa
20	T_{au}	Au tensile stress	103	MPa
21	Y_{au}	Au yield strength	200	MPa
22	ρ_{au}	Au material density	19 300	kg m^{-3}
23	c_{p_Au}	Au heat capacity	130	J kg^{-1} K^{-1}
24	K_{au}	Au thermal conductivity	300	W m^{-1} K^{-1}
25	l_{f_au}	Au latent heat	63.7	kJ kg^{-1}
26	T_{m_Au}	Au melting point	1337	K
27	ρ_{ti}	Ti material density	4600	kg m^{-3}
28	E_{ti}	Ti Young's modulus	110	GPa
29	S_{ti}	Ti Shear modulus	43	MPa
30	υ_{ti}	Ti Poisson's ratio	0.3	—
31	T_{ti}	Tensile strength	235	MPa
32	Y_{ti}	Ti yield strength	140	MPa
33	T_{m_ti}	Ti melting point	1941	K
34	T_o	Room temperature	300	K
35	c_{p_ti}	Ti heat capacity	460	J kg^{-1} K^{-1}
36	K_{ti}	Ti thermal conductivity	22	W m^{-1} K^{-1}
37	l_{f_ti}	Ti latent heat	296	kJ kg^{-1}

Table 2 Summary of calculation results combining eqn (1)–(3) and values from Table 1

Parameters				Value
Pulse width/μs				10
F_o				0.1
Fuse thickness/nm	Fuse width/μm	Input voltage/V	Energy to melt fuse/μJ	Input energy/μJ
100	60	1.3	1.83	95
	40	1.2	1.2	70
	20	1.7	0.610	17
250	60	0.64	4.57	299
	40	0.82	3.05	165
	20	0.88	1.52	11
500	60	0.56	9.15	640
	40	0.59	6.1	340
	20	0.68	3.05	9

Fabrication

The fabrication process involves standard bulk micromachining,[28] shown in sequence in Fig. 3. The first step involves the deposition of 200 nm of low-stress, low pressure chemical vapor deposition (LPCVD) Si_3N_4 on 4 inch 300 μm single-crystal-silicon (SCS) wafers. One side of the wafer was patterned and etched *via* reactive ion etching (RIE) to define ~200 μm by 200 μm regions of bare silicon. Exposure to 20% KOH solution resulted in a self terminating etch that created 80 by 80 μm suspended Si_3N_4 membranes. Titanium (30 nm) and gold layers were sputtered after standard organic cleaning. The Au thickness was varied at 100, 250, and 500 nm in order to vary the current

density required to experimentally burst the membranes. The fuses were then defined using standard photolithography, followed by sequential timed wet etching steps using gold and titanium etchants. The lateral dimensions of the fuses were defined by the mask design as 80 μm long, whereas the width was varied per design as 20, 40, and 60 μm.

Release study devices were assembled in the following fashion. The wafers were diced, creating chips that each contained one membrane. The chips were affixed to Pyrex reservoir pieces *via* UV cured epoxy. The Pyrex reservoir pieces are 2.2 mm thick, 6.5 mm long, 5 mm wide, and drilled to define a cylindrical reservoir with a 3.5 mm diameter (20 μL). The base layer was affixed to the backside of the reservoir piece *via* UV cured epoxy. The devices were filled with a motorized syringe unit (World Precision Instruments, USA) to provide a precise payload volume. The input port was sealed with UV cured epoxy (Dymax, Inc.) after filling the devices. The error for volume loading was estimated as 1 μL. Copper wires were soldered directly on the electric pads, and covered with UV-epoxy to prevent any contamination, and guarantee electrical isolation.

Experimental optimization

The experimental optimization involved testing the fabricated versions of the membrane layer. The fuse devices were placed inside of a transparent plastic container to simulate device activation during release. The membrane was fully immersed in water preventing any bubbles from affecting the experimental results. A probe station (Signatone, USA) was used to connect devices to a high power pulse generator (Hewlett Packard, USA). The current was monitored as the voltage drop across the series resistor and was captured using an oscilloscope (Tektronix, USA) as the pulse was applied. The membrane structures were visually inspected during the experiment using the probe-station stereoscope in order to check if the applied pulse provided enough energy to burst the membrane. The optimization step took place by reducing the voltage necessary to burst a membrane, and then by reducing the width of the pulse. Open circuit conditions were also verified by measuring the electrical resistance using a standard ohmmeter.

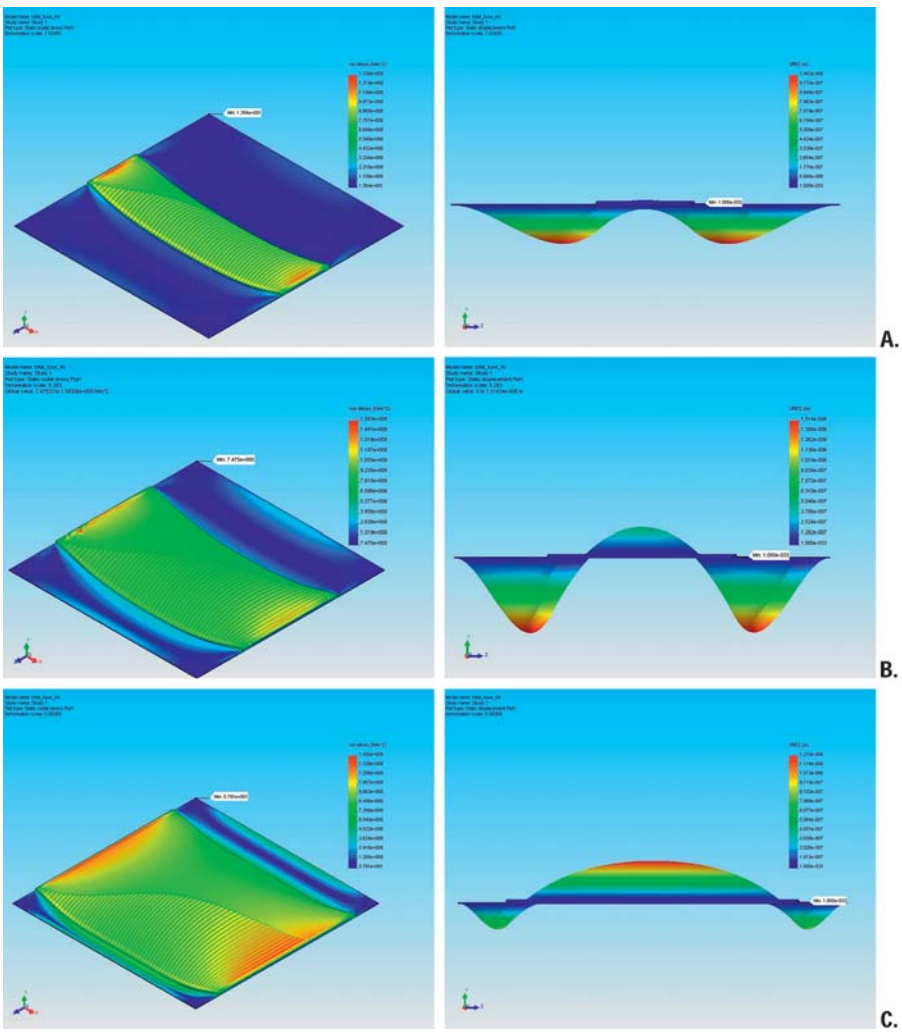

Fig. 2 FEA analysis of the suspended structure showing an isometric view of the Von Mises stress on the surface area of the membrane, and a lateral view for displacement showing structural deformation. The meshed of the analysis included approximately 10E5 elements. (A) 20 μm wide fuse, (B) 40 μm wide fuse, and (C) 60 μm wide fuse.

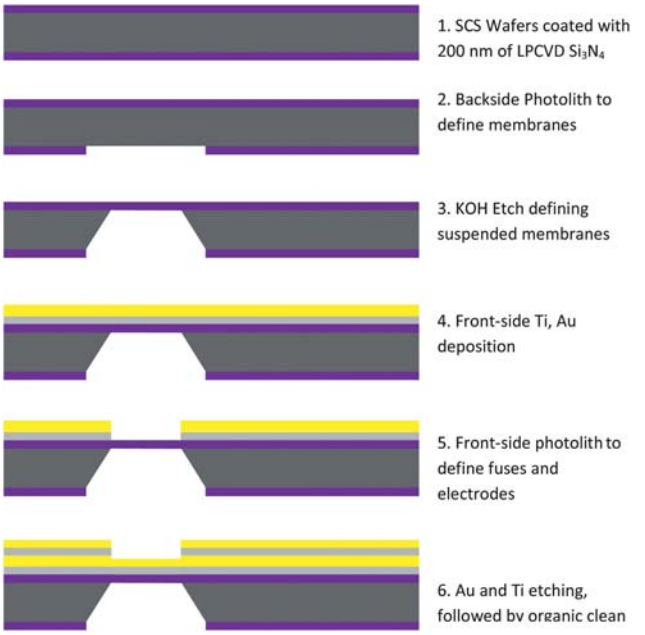

Fig. 3 Fabrication process sequence for the membrane layer and backside input port.

Table 3 Values depicted in Fig. 7, $n = 5$

Number	Width/μm	Thickness/nm	$R_{measured}$/Ω	Time/μs	Energy/μJ
1	60	500	0.5	970	1409
2		250	0.68	250	347
3		100	1.7	58	40
4	40	500	0.52	500	512
5		250	1.01	170	134
6		100	1.7	65	30
7	20	500	1.27	94	78
8		250	1.72	66	40
9		100	3.95	18	14

Table 3 provides a summary of the experimental results, showing the average values per fuse type. Fig. 4 and 5 show a series of SEM, microscope, and confocal microscope images (of membranes per fuse type for a 250 nm thick gold layer prior to and post-activation). The effective area for the 20 μm wide fuse is critically smaller than for the 40 μm and 60 μm wide fuses. The images clearly show that the membranes ruptured, and that the fuses melted. Fig. 5 also shows 3D confocal images of the membranes after fuse activation. The 20 μm wide fuse was partially burst and deformed; whereas for the 40 μm and 60 μm wide fuses, the membranes were fully burst. Fig. 6 shows the voltage and current traces for a 250 nm thick gold layer for each fuse width, captured using the oscilloscope. The pulse height and width of the current decrease as a function of width. Fig. 7 shows a three dimensional plot of the energy required to burst a membrane as function of fuse dimensions. It is possible to observe the energy required to burst the membrane scales down as function of width and thickness, corroborating the theoretical calculations. The voltage and time were also indicated in the 3D plot. 40 μm wide fuses were chosen as the optimal for the release characterization, they are capable of bursting the entire membrane consistently, and maximize the flux area.

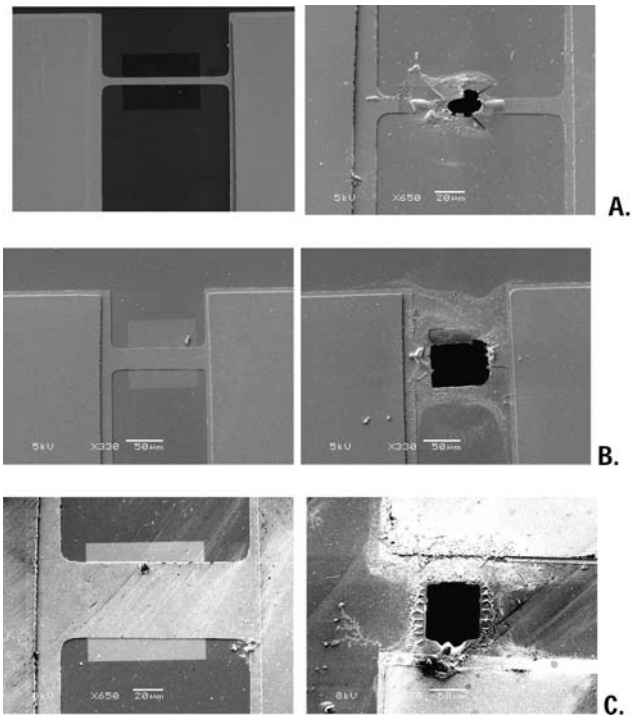

Fig. 4 SEM and confocal microscope images of sealing layer showing structure before and after activation for each fuse dimension all with 250 nm of Au layer. (A) 20 μm wide, (B) 40 μm wide fuse, and (C) 60 μm wide.

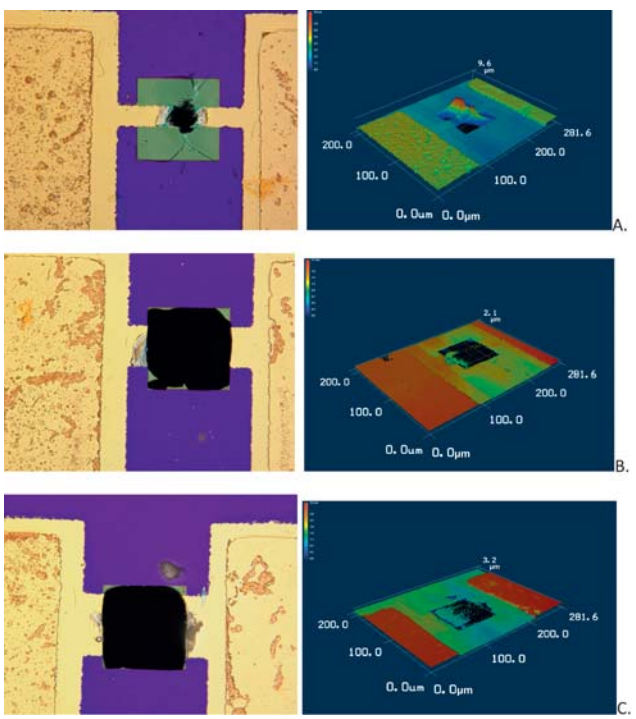

Fig. 5 Microscope and confocal microscope images for 250 nm thick fuses. (A) 20 μm wide, (B) 40 μm wide, and (C) 60 μm wide.

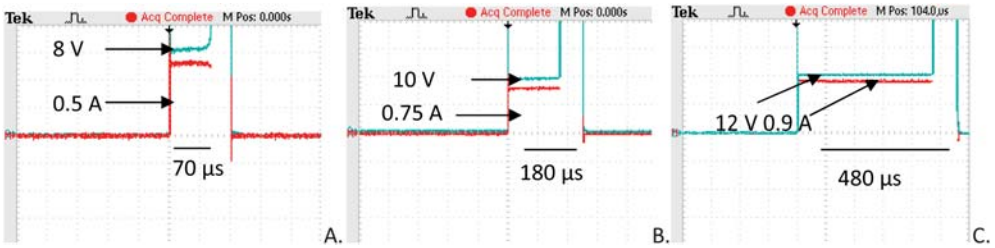

Fig. 6 Oscilloscope capturing images showing activation pulse voltage values (blue) and current (red) values for 250 nm thick fuses. (A) 20 µm wide, (B) 40 µm wide, and (C) 60 µm wide.

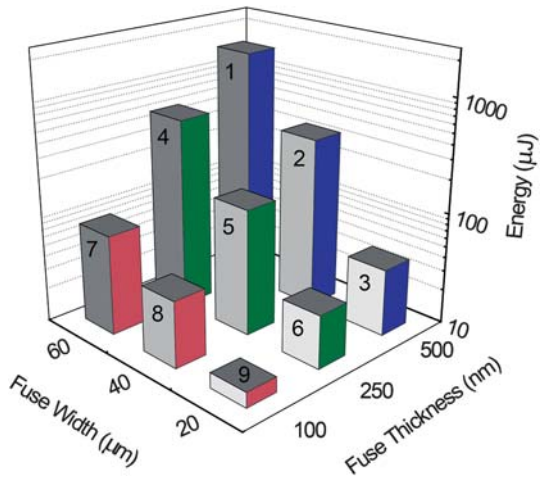

Fig. 7 Minimum energy to burst fuse as a function of fuse dimensions. Refer to Table 3 for values.

Release experiments

The assembled devices were filled (20 ± 1 µL) with a radiolabeled mannitol-C^{14} (Moravek, USA) water solution with a syringe micro-injector. The devices were activated using the high pulse voltage generator at 2 V and pulse width of 250 µs, introducing a factor of safety of approximately 400 percent from the experimental optimization results. Fig. 5 shows the experimental setup. Soon after the devices were activated, the resistance of the fuse was measured to verify open circuit condition, which was verified for all the activated devices. Fig. 1D shows a photograph of the assembled device. The release experiments consisted of using 10 devices, 5 served as un-activated controls and the remaining 5 were activated for release characterization. Each device was placed into a stirred 4 millilitre de-ionized water bath at room temperature. The baths were sampled regularly and the extent of release was quantified using liquid scintillation counter (Perkin Elmer, USA). Fig. 8 is a plot of the average extent of release *versus* time of the activated and control devices. The amount released by each device was normalized to its original payload and plotted as a function of time. The control devices remain at baseline levels for the duration of the study. The activated devices all demonstrated reproducible, diffusion driven release profiles of the form:

$$M(t) = 1 - \exp(-kt) \quad (4)$$

where $M(t)$ is the normalized extent of release (mass released divided by mass loaded), k is a time constant related to the diffusivity and the geometry of the system and t is time. Profiles of this form are consistent with 1st order release from a drug delivery device (see ESI†). The relatively small amount of error present in the release curves demonstrates that gold fuses are capable of rupturing underlying nitride membranes reliably and in a manner that produces a consistent aperture, providing a very repeatable flux.

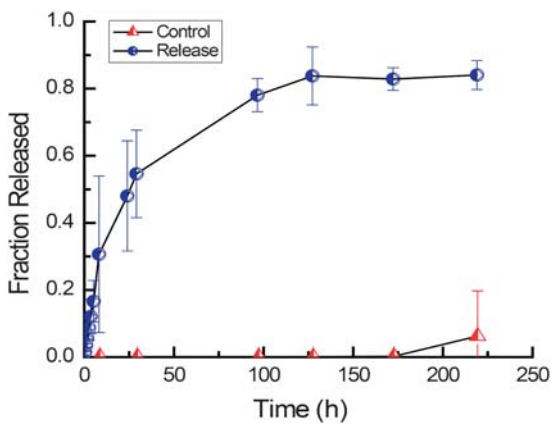

Fig. 8 Release profiles, $n = 5$ for activated devices, and $n = 5$ for control devices. Error bars represent standard deviation.

Discussion

The ETISFA was simulated using a FEA model to provide an analysis of the mechanical behavior of the suspended membrane. Fig. 2 provides a unique insight to understand how the mechanical dimensions of the fuse make an impact on the mechanical deformation of the membrane. The Von Mises stresses and displacements were numerically calculated and plotted. The fuse acts as an electro-thermal actuator that allows for rapid mechanical expansion of the silicon nitride membrane. The width of the fuse is of unique importance to provide the stresses in the critical points of the suspended structure. Fig. 2 also shows the lateral view of the displacement per fuse type as the fuse temperature is defined as the melting point of gold. Three displacement peaks are clearly noticed. The first peak shows how the bending stresses introduce deformation in outward direction. The second and third peaks show how the bending stresses introduce deformation in the inward direction. An interesting aspect of the simulation shows how the magnitudes of the upper

peak displacement and the magnitude of the lower peak displacement increase as a function of the increasing width. It is important to notice the distance between peaks is proportional to fuse width, forcing the peaks closer to the edges as the width increases. Fig. 2 also reveals that the peak sharpness decreases as a function of the increasing width. The simulations provide an understanding for optimization of the fuse width; if the fuse is too narrow, the displacement peak will be sharp but the stress magnitude will not be as high as the widest fuse. If the fuse width is too wide, too much energy will be inefficiently used.

It is important to notice that the static analysis was implemented defining a constant temperature along the surface area of the fuse. The analytical calculations in Table 3 demonstrate that the current density and the pulse width necessary to achieve T_m will scale with fuse width. Fig. 2 shows a perspective on the experimental optimization providing a selection criterion for the device dimensions for reliable *in vitro* and *in vivo* experiments. The thickness plays a key role as the resistance increases with decreasing cross-sectional area, resulting in an increase of the current density. Although less energy is required to melt the fuse, more energy is required to achieve plastic deformation. As a result of this optimization, the chosen fuse dimensions for the release experiments were the intermediate values, 40 μm wide and 250 nm thick, in order achieve a wide and sharp deformation peak that would provide enough energy to completely burst the membrane with the lowest energy.

The previous device generation required approximately 1 J for activation. The energy requirements for activating the ETISFA range from 9 μJ to 640 μJ depending on the fuse geometry (width and thickness), which represents at least a 4 order of magnitude improvement. We utilized the geometry of 40 μm by 250 nm as the exact middle point to achieve low activation energy as well as satisfying the requirement of complete membrane area opening. A previously reported MEMS drug delivery device[29] contains a metallic membrane that upon activation is completely melted by resistive heating. The device required activation energies of 25 μJ, with smaller 50 × 50 μm Pt/Ti/Pt membranes. This opening mechanism, however, does not scale up favorably with dimension because the activation energy scales with the membrane area. The ETISFA, on the other hand, requires only a fraction of the material to burst the membrane, since the failure mechanism is based on locating a narrow fuse at the critical areas of maximum stress values of the membrane, rather than melting the full membrane material.

Table 4 Summary of FEA for maximum stress, deformation levels and FOS as function of temperature and membrane and fuse length

Temperature/K	Fuse dimension/μm	Max. deformation/μm	Max. stress/GPa	FOS (von Mises)
1350	40	.004	2.06	0.097
1350	80	2.08	2.00	0.100
1350	90	2.41	2.09	0.096
1350	100	2.21	2.07	0.097
1350	110	3.00	2.04	0.098
1350	125	3.34	2.07	0.097
1350	150	4.00	2.04	0.098
1350	200	5.60	2.08	0.096
400	40	0.004	2.00	1.00
400	80	0.202	1.93	1.00
400	90	0.234	2.02	1.00
400	100	0.214	2.00	1.00
400	110	0.291	1.98	1.00
400	125	0.325	2.00	1.00
400	150	0.394	1.97	1.00
400	200	0.540	2.00	1.00

FEA analyses were performed in order to obtain a more comprehensive understanding of the fuse activation mechanism and how activation energy scales with membrane size. Simulations were performed for 40 μm wide, 250 nm thick gold fuses that traversed square membranes of varying size. The stress, deformation, and factor of safety based on the Von Mises criterion were calculated. Table 4 provides a summary of the simulations. Simulations were first run with the fuse at 1350 K, just above the melting temperature of gold.

The factors of safety (FOS) based on the Von Mises criterion for fuses at this temperature were approximately 0.1. The next step of the simulations was to perform an optimization for which the FOS was defined as 1 while the temperature on the fuse was varied. Simulations revealed that for all structural lengths, the FOS equaled 1 when the fuse temperature was defined as 400 K. Each membrane failed at the same fuse temperature, width and thickness. The energy required to achieve this temperature, therefore, scales only with the length of the fuse, refer to eqn (1). Another important aspect to take into account is the non-linear scaling of the structural integrity of the membrane. The silicon nitride membrane behaves as brittle material structure with a stiffness and robustness that decreases as a function length, as shown by the following equation:[30–35]

$$P = \frac{C_1 t \sigma_o}{l^2} d + \frac{C_2 E t}{l^4} d^2 \quad (5)$$

where C_1 and C_2 coefficients equal to 3.03 and 0.547 correspondingly, t is thickness, l is width, d is deflection and E is the Young's modulus. The first term defines the pressure to balance the residual stress (σ_o) the membrane. The second one is defined by the stretching of the membrane. The fuse structure has a plastic deformation until it melts with a stiffness and structural robustness that decreases as function length but slightly reinforces the overall structural robustness of the membrane. Therefore, two competing forces need to be taken into account. The first one is the mechanical energy to create a failure mode in a membrane, which decreases as function of length. The second one is the energy to melt a fuse, which increases linearly as function of length. These two considerations need to be combined with the fact that FEA static analysis does not provide information related to the transient time, as well as other non-linear effects due to the spike in the applied electrical signal, and the fact that devices were activated in water. The full elucidation of these effects is beyond the scope of this work and will be addressed in the future work related to the device function. Therefore, the linear scaling argument that resulted from the FEA analyses is an upper bound and provides just a first order approximation of how activation energy scales. Fuses (40 μm × 250 nm) were used to activate devices with an effective aperture of 200 μm × 200 μm. The average activation energy was found to be approximately 70 μJ. Non-linear effects, therefore, appear to dominate the activation energy scaling on this length scale.

The very tight tolerances during manufacturing process assured consistent resistor values that provided repeatable results

for the release experiment. The release curves shown in Fig. 6 provide valuable information on the process that follows almost ideal diffusion curves from a point source. Fig. 6 shows the release experiments during 200 hours of delivery. The control curves demonstrated that the devices were sealed, and did not provide any significant leakage. The tight variations within profiles guarantee a controlled release for drug delivery devices that could be used as novel therapeutic modalities for a wide number of applications. Future work will also include the introduction of higher resistivity materials such as Ti/Pt in order to further minimize the energy consumption.

These results demonstrate that this technology can be employed to produce very effective, reliable and low power MEMS based delivery systems for a number of pharmacological therapies. This device can be a platform for targeted treatment, instead of systemic delivery, providing more efficacious and tolerant treatments with fewer harmful side effects. Special attention will be given to the field of oncology for treatment of inoperable cancers, miniaturized delivery devices are advantageous over traditional treatments.

Conclusion

The motivation for this work was to explore a fuse activation mechanism that operates *via* electro-thermally induced structural failure for miniaturized implantable drug delivery devices capable of on demand activation for controlled release at low energy consumption. The role of fuse dimensions was closely investigated to optimize energy consumption. Two metrics, extent of membrane rupture and energy consumption, were used to evaluate the performance of each fuse type. The fuse mechanism has been optimized to reduce the energy consumption, while maximizing the aperture area for flux. Drug delivery microdevices implemented with this mechanism released mannitol-C^{14} in a controlled, reproducible fashion. Future work will include the development of an analytical model complemented by simulations to obtain an in-depth analysis of the actuator behavior. We will also investigate new materials, including the use of higher resistivity metals. Future work will also involve the use of an *in vivo* model. ETISFA holds promise as a method of achieving on-demand controlled release from MEMS based implantable drug delivery microdevices for a wide range of pharmacological therapies. The ability to control the burst area of the membrane provides a unique method to vary the flux and therefore the release rate on demand. For example, we could envision the use of a single reservoir capped by a number of membranes. Each membrane can be addressed independently and ultimately provide a variable flux. Therefore, the ETISFA could have a potential in the field of personalized medicine for which a dose could be dynamically customized per patient and as function of dynamic diagnosis. We believe that there are great ramifications for the potential use of ETISFA as devices for new drug delivery modalities that will involve the use of long term implantation for treatment of acute conditions as well as chronic illnesses.

Acknowledgements

This research work was partially supported by the National Institute of Health (NIH Grant: EB006365), and the US Army Research Office *via* the Institute for Soldier Nanotechnologies (ISN) at MIT (contract: W911NF-07-D-0004).

References

1 N. M. Elman, Y. Patta, A. W. Scott, B. Masi, H. L. Ho Duc and M. J. Cima, The next generation of drug-delivery microdevices, *Clin. Pharmacol. Ther.*, 2009, **85**(5), 544–547.
2 Y. Li, R. S. Shawgo, B. Tyler, P. T. Henderson, J. S. Vogel, A. Rosenberg, P. B. Storm, R. Langer, H. Brem and M. J. Cima, *In vivo* release from a drug delivery MEMS device, *J. Controlled Release*, 2004, **100**, 211–219.
3 Y. Li, H. L. Ho Duc, B. Tyler, T. Williams, M. Tupper, R. Langer, H. Brem and M. J. Cima, *In vivo* delivery of BCNU from a MEMS device to a tumor model, *J. Controlled Release*, 2005, **106**, 138–145.
4 A. C. R. Grayson, R. Scheidt Shawgo, Y. Li and M. J. Cima, Electronic MEMS for triggered delivery, *Adv. Drug Delivery Rev.*, 2004, **56**(2), 173–184.
5 N. M. Elman, H. L. H. Duc and M. J. Cima, An implantable MEMS drug delivery device for rapid delivery in ambulatory emergency care, *Biomed. Microdevices*, 2009, **11**(3), 625–631.
6 N. M. Elman and U. M. Upadhyay, Medical applications of implantable drug delivery microdevices based on MEMS (Micro-Electro-Mechanical-Systems), *Curr. Pharm. Biotechnol.*, 2010, **11**(4), 398–403(6).
7 M. A. Moses, H. Brem and R. Langer, Advancing the field of drug delivery: taking aim at cancer, *Cancer Cell*, 2003, **4**, 337–341.
8 S. Brem, B. Tyler, K. Li, G. Pradilla, F. Legnani, J. Caplan and H. Brem, Local delivery of temozolomide by biodegradable polymers is superior to oral administration in a rodent glioma model, *Cancer Chemother. Pharmacol.*, 2007, **60**, 643–650.
9 R. Langer, Where a pill won't reach, *Sci. Am.*, 2003, **288**, 50–57.
10 J. T. Santini, M. J. Cima and R. Langer, A controlled-release microchip, *Nature*, 1999, **397**(6717), 335–338.
11 J. T. Santini, A. C. Richards, R. A. Scheidt, M. J. Cima and R. S. Langer, Microchip technology in drug delivery, *Ann. Med.*, 2000, **32**(6), 377–379.
12 A. C. R. Grayson, I. S. Choi, B. M. Tyler, P. P. Wang, H. Brem, M. J. Cima and R. Langer, Multi-pulse drug delivery from a resorbable polymeric microchip device, *Nat. Mater.*, 2003, **2**, 767–772.
13 J. H. Prescott, S. Lipka, S. Baldwin, N. F. Sheppard, Jr, J. M. Maloney, J. Coppeta, B. Yomtov, M. A. Staples and J. T. Santini, Jr, Chronic, programmed polypeptide delivery from an implanted, multireservoir microchip device, *Nat. Biotechnol.*, 2006, **24**(4), 437–438.
14 M. Armand and J. M. Tarascon, Building better batteries, *Nature*, 2008, **451**(7179), 652–657.
15 J. M. Tarascon and M. Armand, Issues and challenges facing rechargeable lithium batteries, *Nature*, 2001, **414**(6861), 359–367.
16 N. Nathan, Battery technologies for biomedical microdevices, *Curr. Pharm. Biotechnol.*, 2010, **11**(4), 404–410(7).
17 A. M. Cardenas-Valencia, J. Dlutowski, J. Bumgarner, C. Munoz, W. Wang, R. Popuri and L. Langebrake, Development of various designs of low-power, MEMS valves for fluidic applications, *Sens. Actuators, A*, 2007, **136**(1), 374–384.
18 M. L. Cardenas, A. M. Cardenas-Valencia, J. Dlutowski, J. Bumgarner and L. Langebrake, A finite element method modeling approach for the development of metal/silicon nitride MEMS single-use valve arrays, *J. Micromech. Microeng.*, 2007, **17**(8), 1671–1679.
19 G. Voskerician, M. S. Shive, R. S. Shawgo, H. von Recum, J. M. Anderson, M. J. Cima and R. Langer, Biocompatibility and biofouling of MEMS drug delivery devices, *Biomaterials*, 2003, **24**(11), 1959–1967.
20 J. Yota, J. Hander and A. A. Saleh, A comparative study on inductively-coupled plasma high-density plasma, plasma-enhanced, and low pressure chemical vapor deposition silicon nitride films, *J. Vac. Sci. Technol., A*, 2000, **18**(2), 372–376.
21 W. P. Eaton, F. Bitsie, J. H. Smith and D. W. Plummer, A New Analytical Solution for Diaphragm Deflection and its Application to a Surface-micromachined Pressure Sensor, *1999 International Conference on Modeling and Simulation of Microsystems*, 1999, pp. 640–643.

22 D. Maier-Schneider, J. Maibach and E. Obermeier, A new analytical solution for the load-deflection of square membranes, *J. Microelectromech. Syst.*, 1995, **4**(4), 238–241.
23 G. Kotzar, M. Freas, P. Abel, A. Fleischman, S. Roy, C. Zorman, J. M. Moran and J. Melzak, Evaluation of MEMS materials of construction for implantable medical devices, *Biomaterials*, 2002, **23**(13), 2737–2750.
24 J. S. Lee, D. S. W. Park, A. K. Nallani, G. S. Lee and J. B. Lee, Sub-micron metallic electrothermal actuators, *J. Micromech. Microeng.*, 2005, **15**(2), 322–327.
25 D. Maier-Schneider, S. Kolb, B. Winkler and W. M. Werner, Novel surface-micromachined low-power fuses for on-chip calibration, *Sens. Actuators, A*, 2002, **97–98**, 173–178.
26 C. B. Picallo and J. M. Lopez, Energy dissipation statistics in the random fuse model, *Phys. Rev. E: Stat., Nonlinear, Soft Matter Phys.*, 2008, **77**(4), 046114.
27 Y. S. Chiu, K. S. Chang, R. W. Johnstone and M. Parameswaran, Fuse-tethers in MEMS, *J. Micromech. Microeng.*, 2006, **16**(3), 480–486.
28 N. M. Elman, S. Krylov, M. Sternheim and Y. Shacham-Diamand, Multiple aspect-ratio structural integration in single crystal silicon (MASIS) for fabrication of transmissive MOEMS modulators, *Microsyst. Technol.*, 2008, **14**(2), 287–293.
29 J. M. Maloney, S. A. Uhland, B. F. Polito, N. F. Sheppard, Jr, C. M. Pelta and J. T. Santini, Jr, Electrothermally activated microchips for implantable drug delivery and biosensing, *J. Controlled Release*, 2005, **109**(1–3), 244–255.
30 J. J. Vlassak and W. D. Nix, A new bulge test technique for the determination of Young's modulus and Poisson's ratio of thin films, *J. Mater. Res.*, 1992, **7**(12), 3242–3249.
31 V. A. Gridchin, V. V. Grichenko, V. M. Lubimsky and A. V. Shaporin, Stresses near the edges of a square silicon membrane, *Russian Microelectronics*, 2005, **34**(4), 252–258; (*Mikroelektronika*, 34((3)), 302–310).
32 C. van Rijn, M. van der Wekken, W. Nijdam and M. Elwenspoek, Deflection and maximum load of microfiltration membrane sieves made with silicon micromachining, *J. Microelectromech. Syst.*, 1997, **6**, 48–54.
33 M. G. Ailen, M. Mehregany, R. T. Howe and S. O. Senturia, Microfabricated structures for the *in situ* measurement of residual stress, Young's modulus, and ultimate strain of thin films, *Appl. Phys. Lett.*, 1987, **51**(4), 241–243.
34 S. Timoshenko and S. Woinowsky-Krieger, *Theory of Plates and Shells*, McGraw-Hill Book Co., 2nd edn, 1959, vol. 5–7, pp. 105–257.
35 S. Testu, J.-L. Besson, T. Rouxel and G. Bernard-Granger, Ductility and stress relaxation kineticsin a silicon nitride ceramic in the 1400–1650 °C range, *J. Mater. Sci. Lett.*, 2000, **19**, 1007–1010.
36 W. D. Nix, Mechanical properties of thin films, *Metall. Trans. A*, 1989, **20**(11), 2217–2245.
37 F. R. Brotzen, Mechanical testing of thin films, *Int. Mater. Rev.*, 1994, **39**(1), 24–45.
38 S. F. Pugh, XCII. Relations between the elastic moduli and the plastic properties of polycrystalline pure metals, *Philos. Mag.*, 1954, **45**(367), 823–843, Series 7.
39 M.-A. Nicolet, Diffusion barriers in thin films, *Thin Solid Films*, 1978, **52**(3), 415–443.
40 J. A. Thornton and D. W. Hoffman, Stress-related effects in thin films, *Thin Solid Films*, 1989, **171**(1), 5–31.

